INL/JOU-18-51051-Revision-0

Using Computational Fluid Dynamics of Wind Simulations Coupled With Weather Data to Calculate Dynamic Line Ratings

June 2019

Alexander W Abboud, Jake P Gentle, Timothy R McJunkin, Jacob P Lehmer

Changing the World's Energy Future

INL is a U.S. Department of Energy National Laboratory operated by Battelle Energy Alliance, LLC

INL/JOU-18-51051-Revision-0

Using Computational Fluid Dynamics of Wind Simulations Coupled With Weather Data to Calculate Dynamic Line Ratings

Alexander W Abboud, Jake P Gentle, Timothy R McJunkin, Jacob P Lehmer

June 2019

Idaho National Laboratory
Idaho Falls, Idaho 83415

http://www.inl.gov

Prepared for the
U.S. Department of Energy
Under DOE Idaho Operations Office
Contract DE AC07-05ID14517

Using Computational Fluid Dynamics of Wind Simulations Coupled with Weather Data to Calculate Dynamic Line Ratings

Alexander W. Abboud[1*], Jake P. Gentle[1‡], *Senior Member IEEE*, Timothy R. McJunkin[1], *Senior Member IEEE*, Jacob P. Lehmer[1], *Member IEEE*
[1] Idaho National Laboratory, 1955 N., Freemont Ave, Idaho Falls, ID, USA
Corresponding Emails: *Alexander.Abboud@inl.gov, ‡Jake.Gentle@inl.gov

***Abstract*—Dynamic line rating is a technology that allows for the rating of electrical conductors to be calculated based on local weather conditions rather than using "worst-case" assumptions of weather conditions. The static ratings are typically based on weather conditions that are conservative in nature, and thus dynamic line rating may provide room to increase the current capacity. The local weather conditions may estimate conditions more accurately near the transmission lines accounting for terrain such as nearby hills. One way to estimate the local weather conditions is through the use of computational fluid dynamics. The results of a wind field simulation can be coupled with sparsely located weather stations to provide an accurate assessment of the wind speeds along the path of the conductor. The wind field simulations are calculated using a steady state Reynolds-averaged Navier-Stokes model. These results along with local solar irradiance measurements can be used to provide estimates of the steady state ampacity with the standard IEEE equations. An advanced test case for this process involves performing these simulations in a complex terrain, Hells Canyon, the deepest river gorge in North America. The results show that by using weather-based sensors without considering localized wind conditions, the available ampacity may be over-predicted significantly.**

***Index Terms*—Dynamic line rating, general line ampacity state solver, computational fluid dynamics, overhead transmission lines**

I. Introduction

For the determination of the current carrying capacity of a conductor for transmission lines, the limiting factor is typically the temperature of the lines which cause increased amount of sag of a span between structures from thermal expansion at high temperatures, or even annealing of conductors at extreme temperatures. Typically, the capacity of transmission lines on the grid are calculated using a single static rating, or seasonally adjusted static rating [1]. The static ratings use conservative estimates - low wind, high ambient temperature, high solar irradiance - based on seasonal conditions, and consequently these conservative calculations can underestimate the actual capacity due to cooling effects of the environment. Dynamic Line Ratings (DLR) can be used to defer upgrades, increase the yield of distributed generation and support the network during outages. DLR has been identified as a key transmission and distribution infrastructure solution by the United States Department of Energy [2, 3]. The maximum steady state current on a overhead transmission is well characterized from the International Council on Large Electric Systems (CIGRE) [4], the International Electrochemical Commission (IEC) [5], and the Institute of Electrical and Electronics Engineers (IEEE) [6, 7]. Studies into DLR have shown potential for day ahead planning [8], or as a way for easing congestion of lines [9, 10]. Natural synergy with increased wind power generation coupled with thermal cooling also provides large benefits to promote integration with DLR technology [11–14] Results of analyzing collected weather data in the field has shown potential to increase ampacity above static for for case studies in Canada [15, 16], the US and the UK [17] and forecasted weather data in Ireland [18].

This study examines the use of computational fluid dynamics (CFD) in order to predict wind speeds and incident direction along a transmission line. These wind speeds can subsequently be used in calculations of the current capacity of overhead transmission lines. The wind speeds only contribute towards one aspect of the calculation. The capacity is an energy balance between the environmental conditions for convective cooling, thermal radiative cooling and heating from the Joule effect and solar radiance. For this study, the steady state equation for the transmission line ampacity is used. This assumption of steady state can be made due to the separation of the time scales, with overhead conductors typically requiring 10-20 minutes for a change in the temperature [4, 19] depending on the size of the conductor.

For the large-scale wind simulations in this study, the steady state Reynolds-averaged Navier-Stokes (RANS) approach is used [20]. As with the assumption of the thermal conductor timescales, the time scale of the weather patterns is assumed to not change rapidly enough to require an unsteady RANS approach or a more accurate (and more computationally expensive) large eddy simulation (LES). This allows the

This research was completed by Idaho National Laboratory with funding from the U.S. Department of Energy Wind Energy Technologies Office, and support from Phil Anderson and Shane Woods at Idaho Power Company, and Catherine Meissner of WindSim AS. Idaho National Laboratory is operated by Battelle Energy Alliance under contract No. DE AC07-05ID14517.

total computational time to remain manageable. The RANS approach has been shown to be accurate for wind field simulations when mapping weather station data to extrapolated locations with lookup tables in relation to actual weather data observations [17]. As the convective cooling rate is calculated as a function of the wind speed raised to the power of 0.52 or 0.6, then a 10% error in wind speed translates to about 5-6% error in the forced convective cooling rate.

Some studies have shown the RANS equations may not be sufficient for hilly terrain, as the downstream regions after crossing hills may produce over-predictions of the speed up ratios [21]. The predictions between RANS and experimental data show better agreement with the windward part of the sites rather than the leeward part in more complex flows [21]. However, the WindSim CFD software has been utilized for the calculation of wind fields using the RANS turbulence modeling, and has been validated in complex terrain [22, 23]. Wind speed accuracy with RANS flow has been used by Milashuk and Crane [24] for the evaluation of wind resource predictions and accuracy assessment by transforming measurements at a reference location to other locations of interest, and similar wind mapping has been completed on low-elevation mountains by Dhunny et al. within acceptable validation error [25, 26]. The application here is quite different, but the methodology of mapping CFD and recorded weather station observation data to specific locations remains similar.

The use of CFD in the calculation of DLR has several significant advantages over other methods. First off, the CFD is calibrated against known weather data so that the wind speeds should be accurate. If weather stations were to be installed at each structure location over a given area of interest the cost would be quite prohibitive. The interpolation of the CFD wind speeds to specific locations between the sparsely installed weather stations can provide regions where wind speeds may be lower due to terrain effects that would otherwise go unnoticed. This gives a more conservative estimate of the DLR calculation along a given transmission line. Second, the combination of utilizing the CFD results with installed weather stations can be more cost effective than other measurement techniques such as direct temperature measurements or sag installation devices, and weather station installation requires no outage period of the transmission line. Thirdly, by coupling weather stations with CFD for analysis of historical data, this provides some validation in the methodology here to eventually be used for predictive or forecasted line ratings, which have more potential for cost benefits than real time ratings. Lastly, even if it is desired to use direct measurement devices for determining the dynamic line rating rather than weather station data, the CFD results can be used to identify the limiting midpoints of line segments in terms of cooling capacity. These line segments would then be the desired locations for placements of direct measurement devices.

This site is of interest contains several hydroelectric dams important for power generation. The power delivery out of this region is important as the calculated line ampacity calculations may change depending on higher wind gusts on ridges versus regions along the river where steep hills may block wind from efficiently cooling the lines. This study first shows the terrain and transmission line locations for the study, followed by a brief summary of the theory for CFD and steady state conductor calculations. Then the CFD flow field results are shown, and the results of running the General Line Ampacity State Solver (GLASS) code developed by INL to determine the dynamic rating on the line segments over the 1-year historical time period. The data from the extrapolated weather station to midpoint locations is also analyzed to find the critical midpoint segments within the terrain that limit the line's overall dynamic ampacity rating.

II. Terrain of Trial Site

The geographic location for this site is a complex region, Hells Canyon, the deepest river gorge in North America. The site is located along the border of Idaho and Oregon. The Snake River flows 1600 meters below the west rim, and 2300 meters below the mountain peaks to the east. The exact region of interest extends 30 kilometers in the east-west direction and 60 kilometers in the north-south direction. Digital elevation model (DEM) data was obtained from the national database for the region in latitude-longitude sets with a spatial resolution of 30 meters, shown in Fig. 1. Transmission line structure location data were provided for the region from the controlling power company.

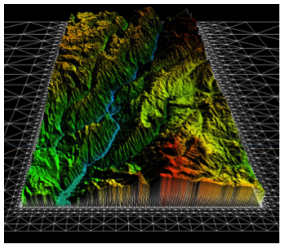

Fig. 1. Three-dimensional image of Hells Canyon terrain extent. The river runs roughly in the center of the east-west extent.

The raw DEM and transmission line structure data must be transformed into a linear Universal Transverse Mercator (UTM) projection to be used within the CFD code. Due to the large physical size of the area, near ground effects are not resolved within the CFD simulations. The terrain data is used to calculate a normalized roughness layer from 0 to 1 in order to model the subgrid effects such as shrubs, trees and buildings. The roughness layer of the terrain is shown in Fig. 2a. This value is set to 1.0 for city regions (dark red on the scale), 0.8 for heavily forested areas (red on the scale), 0.1 - 0.2 for farmland or plains covered in shrubs (yellow on the scale), and set to 0 (white on the scale) for flat areas, such as along the water surface, and for areas with very little vegetation. The roughness values are used in the log-law correlations for the boundary layer with values adapted from Troen and Petersen [27]. The elevation of the region is shown in Fig. 2b with very large variation from the river to the mountains on either side.

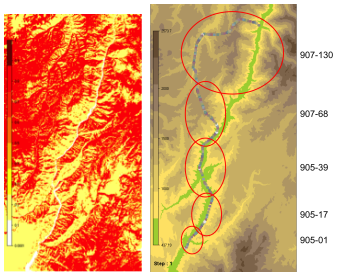

(a) (b)

Fig. 2. (a) shows the roughness layer of terrain, this is normalized to scale from 0 to 1, (b) shows the map of the transmission line structures and weather station locations and the segmentation of the line.

In this prescribed region there are 160 transmission line structures along the full transmission line that are investigated. While there are more in the region, the study is focused solely on one of these transmission lines. The locations of the transmission line structures and five weather stations in the region are shown in Fig. 2b. The square markers on the terrain plot show the path of the transmission line of interest, and the circles show the weather station locations. The installed weather stations record data internally with 3-minute intervals. To separate out the analysis the line is divided into five separate segments based on the nearest weather station, these are circled and labeled in Fig. 2b. The northern portion of the canyon originally had two additional weather stations installed, but upon data retrieval, these were found to be inoperable for most of the time period, which may subject the northern region results to larger error than the southern region.

III. Methodology

A. Computational Fluid Dynamics Simulations

For the CFD simulations, the commercial software WindSim 8.0 was used for full three-dimensional results. The domain for the simulation was created by making an x-y mesh with the same 30-meter resolution provided by the DEM data. For the vertical direction non-uniform spacing was used in order to provide better near ground resolution for more accurate wind speeds near transmission lines. A 5-meter resolution was used from ground level up to 50 meters, a 10-meter resolution was used up to 100 meters, and a growing pseudo-logarithmic spacing was used up to 3500 meters. A 10 m/s boundary condition is applied at the boundary layer height, a prior study showed that the sensitivity to this boundary condition is minor when coupled with available weather data in resource assessment [22], and significantly lower ground speeds are to be expected in the model. The mesh of the entire region is shown in Fig. 3, it contains approximately 85 million cells. However, due to the computational limitations of the machine and CFD code, the entire domain is split in the north-south direction and two separate domains are constructed of over 50 million cells each. Due to the large elevation differences, the vertical mesh can become skewed in several places. The linear UTM 11 projection that was used on the DEM data provides simple importing of the terrain into the CFD code.

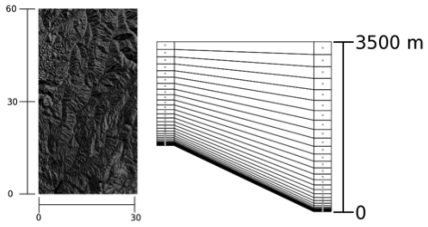

(a) (b)

Fig. 3. Horizontal (a) and vertical (b) mesh layout, which shows the skewed mesh from high peaks to the low river elevation.

A method referred to as Wind Atlas is used to piece together results from the boundaries of the two domains. This method has been demonstrated over extremely large areas with the WindSim CFD code previously for mapping out the wind fields in Switzerland [28]. When large elevation changes occur near the boundaries for CFD simulations there can be potential for unphysical speedups to occur due to the recirculation zones. Often these can be dampened by placing boundaries far from changes in the geometry, but is not an option here with the pathway of the transmission line. The partial differential equations dictating the wind field solution for the Reynolds-averaged Navier-Stokes equations with the standard $k-\epsilon$ method that is used are the three velocity vectors, U_i, the turbulent kinetic energy, k, and the turbulent dissipation rate, ϵ, given by:

$$\rho U_i \frac{\partial U_j}{\partial x_i} = \frac{\partial}{\partial x_i}\left[(\mu+\mu_t)\left(\frac{\partial U_i}{\partial x_j}+\frac{\partial U_j}{\partial x_i}\right)\right] - \frac{\partial p}{\partial x_i} \tag{1}$$

$$\begin{aligned} \frac{\partial (U_i k)}{\partial x_i} &= \frac{\partial}{\partial x_i}\left(\frac{\mu_t \partial k}{\sigma_k \partial x_i}\right) + P_k - \epsilon \\ \frac{\partial (U_i \epsilon)}{\partial x_i} &= \frac{\partial}{\partial x_i}\left(\frac{\mu_t \partial \epsilon}{\sigma_\epsilon \partial x_i}\right) + c_{\epsilon 1}\frac{\epsilon}{k}P_k - c_{\epsilon 2}\frac{\epsilon^2}{k} \end{aligned} \tag{2}$$

where ρ is the air density, x_i are the position coordinates, p is the pressure, μ is the viscosity, and C_μ, $c_{\epsilon 1}$, $c_{\epsilon 2}$, σ_k and σ_ϵ are the fixed constants for the $k-\epsilon$ model, with values set to 0.09, 1.55, 2.0, 1.0 and 1.3, respectively [20]. The two other terms are the turbulent viscosity, μ_t, given by:

$$\mu_t = \frac{C_\mu k^2}{\epsilon} \tag{3}$$

and the turbulent production term, P_k, given by:

$$P_k = \mu_t \left(\frac{\partial U_i}{\partial x_j}+\frac{\partial U_j}{\partial x_i}\right)\frac{\partial U_i}{\partial x_j}\,. \tag{4}$$

B. Conductor Rating Calculation Method

The line ratings are calculated for steady state conditions every 3 minutes, the rate at which weather station data is collected. The wind speed is only one piece of the calculation. Other environmental factors are accounted for, namely, the solar irradiance, ambient temperature, and wind direction. The equations and methodology are documented in the IEEE Standard 738 [6]. The steady state current capacity is calculated by the heat balance by

$$I = \sqrt{\frac{q_c + q_r - q_s}{R(T_c)}} \tag{5}$$

where q_s, q_c, and q_r are the heating though solar radiation, the cooling through convection, and the cooling through radiation; T_c is the conductor temperature, and R is the resistance of the line. It is assumed that radial temperature differences are minor, so that T_c is the same as the line's surface temperature. The radiated heat loss rate per unit length of the transmission line in units of W/m is calculated by

$$q_r = 17.8 D \epsilon_c \left[\left(\frac{T_c + 273.15}{100} \right)^4 - \left(\frac{T_a + 273.15}{100} \right)^4 \right] \tag{6}$$

where ϵ_c is the conductor emissivity, D is the conductor diameter, and T_a is the ambient air temperature in Celsius. In the normal IEEE standards, the heat gain from the sun through solar irradiance is calculated by

$$q_s = \alpha Q_{se} \sin(\theta) A' \tag{7}$$

where α is the solar absorptivity, Q_{se} is the total solar and sky radiated heat flux corrected by elevation, θ is the effective angle of incidence of the suns rays and A' is the projected area of conductor per-unit length. However, for the calculation of static line rating here, and the use of the GLASS ampacity solver code, the installations of the weather stations can be taken advantage of and used for the solar irradiance directly, which will account for cloud cover, terrain shadows and other effects. The convective heat loss per unit length is calculated using one of two equations based on the air speed. For low air speed, under 1.34 m/s (3 mph) the term is given by

$$q_{c1} = \left[1.01 + 1.35 \left(\frac{D V_w \rho_f}{\mu_f} \right)^{0.52} \right] k_f K_{\text{angle}} (T_c - T_a) \tag{8}$$

and for higher air speed the convective heat loss is given by

$$q_{c2} = 0.754 \left(\frac{D V_w \rho_f}{\mu_f} \right)^{0.6} k_f K_{\text{angle}} (T_c - T_a) \tag{9}$$

where V_w is the speed of the air, K_{angle} is the wind direction factor, and the fluid parameters density, ρ_f, viscosity, μ_f, and thermal conductivity, k_f, are calculated at the film temperature ($T_f = (T_c + T_a)/2$). Due to the high variability of the terrain, the air density is calculated as a function of elevation as well, as the parameter can vary as much as 20% over the entire transmission line segment. The wind direction factor is based on the angle between the wind direction and the conductor azimuth for each midpoint segment as

$$K_{\text{angle}} = 1.194 - \cos(\phi) + 0.194 \cos(2\phi) + 0.368 \sin(2\phi) \tag{10}$$

where ϕ is the angle of incidence between the wind direction and the midpoint azimuth – with maximum value of 90 degrees. The convective cooling rates are compared to the natural convective heat loss rate given by

$$q_{cn} = 3.645 \rho_f^{0.5} D^{0.75} (T_c - T_a)^{1.25} \tag{11}$$

and the highest of the heat loss rates is used as q_c in the equation for the ampacity. These calculations are repeated for every midpoint in the region. For each line segment only the lowest midpoint value of the steady state calculation is used in determined the ampacity of the line segment. Lookup tables are created for each midpoint using the WindSim code, and these lookup tables are fed together with the recorded historical data through the GLASS code developed by INL to determine the ampacity. Since the wind near ground level is a boundary layer flow, the results should be self-similar so that for each wind direction one simulation can give an effective solution that is then scaled by real time conditions. The methodology here is applied to historical weather observations, but should be applicable to real-time dynamic line rating calculations as well using it for forecasted ratings [29].

C. GLASS Overview

The program referred to as GLASS is used for the analysis of the historical data in combination with the CFD generated data from WindSim. The main components which are used in the analysis presented in this paper are the CFD portion, which utilizes the WindSim CFD code, scripts for processing the historical data of wind speed, wind direction, solar irradiance, and ambient temperature into a database, and GLASS which solves the equations in Section III-B for every historical database entry to calculate final values for the ampacity rating. Assumptions are made in GLASS such that weather station coverage is sufficient to use nearest neighbor approximations for ambient temperature and solar irradiance values at each midpoint span, with no elevation correction. The advantage to GLASS is that it has been built in such a way that it can provide ampacity estimations for every midpoint span along numerous line sections simultaneously, while also allowing for time-syncing of measured weather station data.

IV. Results

A. Flow Field Results

The CFD simulations are each run 12 times, once for each 30 degree sector of incoming wind direction. For brevity only a few of the wind directions are shown for the flow field images. In Fig. 4 the Northern half of the domain is shown for the incoming wind sector at 0 degrees. The heights shown in this figure vary from 10 m to 50 m to 100 m above the ground level. The same plots for the southern half of the domain are shown in Fig. 5. The wind speeds in both sections of the terrain show a drastic slow down in the predicted wind speeds at 100 meters above ground level down to the 10-meter height where the transmission line structures are located. At this low height where transmission lines are located, the wind speeds in the model are much lower than the boundary layer condition, as shown in Fig. 4a and 5a.

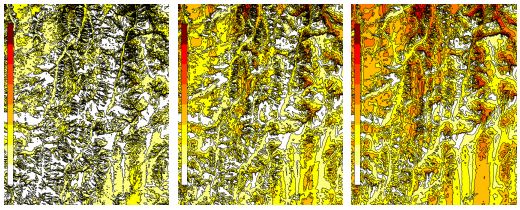

(a) (b) (c)

Fig. 4. Wind speed for the northern terrain section at 0 degree incoming wind sector at 10 m (a), 50 m (b) and 100 m (c) heights.

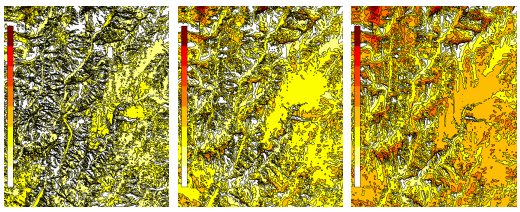

(a) (b) (c)

Fig. 5. Wind speed for the southern terrain section at 0 degree incoming wind sector at 10 m (a), 50 m (b) and 100 m (c) heights.

The wind speed for the incoming flow at 180 degrees for the northern section of the terrain is shown in Fig. 6, and for the southern section of the terrain in Fig. 7. As with the prior plots the wind speeds are shown at 10 m, 50 m and 100 m above ground level. In the 180 degree incoming wind sector the same trend is seen where terrain features cause significant slowing of the wind speed at the 10 m elevation, as shown in Fig. 6a and 7a. At the edge of the simulations, significant speed up of the wind occurs from the incoming wind sector from the north at wind sector 0, and from the south at wind sector 180. This is due to the nearby inlet boundary condition from the incoming wind vector, in cases where terrain is uneven boundary effects can be exacerbated. This effect is mitigated however by placing the boundaries far enough from the transmission line structures of interest, and through the Wind Atlas method, which overlaps the northern and southern sections to use the wind data appropriately to mitigate this.

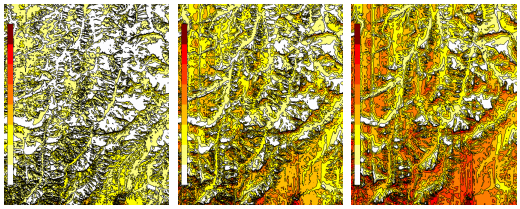

(a) (b) (c)

Fig. 6. Wind speed for the northern terrain section at 180 degree incoming wind sector at 10 m (a), 50 m (b) and 100 m (c) heights.

While not shown, the other 10 wind sectors show similar traits, where due to the large elevation differences blocking effects from terrain on the wind speed are quite pronounced at 10 meters above the ground level elevation. This the typical height of the midpoint of the transmission line between structures, where the wind data is subsequently used in the lookup tables for ampacity calculations in GLASS. In addition, local ground cover from trees and vegetation can affect the

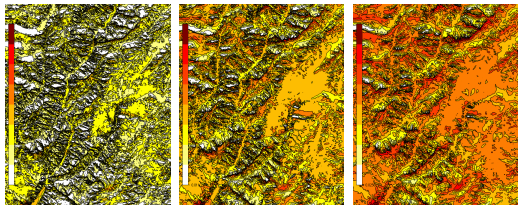

(a) (b) (c)

Fig. 7. Wind speed for the southern terrain section at 180 degree incoming wind sector at 10 m (a), 50 m (b) and 100 m (c) heights.

wind speed in the near-ground levels through the normalized roughness quantity.

In order to assess the accuracy of the wind flows, the data from the transferred lookup tables is compared. The data from each weather station and the appropriate speed up/down and wind direction shift is compared to the actual weather data collected at the next nearest weather station. The summary of the accuracy of the wind speeds in doing this approach is summarized in Table I with the root mean square error (RMSE), along with the distance between the stations. No strong correlation is seen in accuracy of either distance or height, likely due to complex terrain interactions, and far distances between stations. As a steady state simulation is being applied to the transient nature of the wind this large distance between weather stations likely influences this error. There is some threshold distance in which this steady state assumption of wind flow breaks down for the comparison. Additional weather stations should be installed (as mentioned in Sec. II) to improve accuracy. In addition, the influence of the uncertainty of the wind speed is assessed for the ampacity calculation of this line. The ampacity is calculated at each weather station, then compared to the ampacity calculated when using the wind speed change and direction shift from the data of the next nearest weather station. The data for the mean absolute error of the ampacity are shown in Table II, and is further broken down for only the points in time when the wind speed is below the static assumption of 3 mph. The error in the ampacity is about half as much at low wind speeds than at high wind speeds, giving more confidence to the method when utilized for low wind speeds.

TABLE I
WEATHER STATION COMPARISON TO ASSESS CFD ACCURACY.

Weather Station 1	Weather Station 2	Distance (km)	Height Difference (m)	Wind Speed RMSE (m/s)
WS01	WS17	6.6	157	2.61
WS17	WS39	10.9	-259	1.93
WS39	WS68	9.5	509	1.70
WS68	WS130	18.2	49	2.57

B. GLASS Ampacity Calculation

The entire transmission line studied uses the same conductor, so the limiting ampacity is not dependent on the choice of conductor for individual line sections. For the sake of comparison this continuous conductor is divided into five

TABLE II
WEATHER STATION COMPARISON TO ASSESS AMPACITY ERROR FROM WIND SPEED DATA.

Weather Station 1	Weather Station 2	Ampacity Error (A)	Ampacity Error ($<$ 3 mph) (A)
WS01	WS17	210.7	104.9
WS17	WS39	213.3	110.9
WS39	WS68	108.6	59.0
WS68	WS130	205.1	119.7

separate sections based on the nearest weather station to the midpoint span. With the conductor spit into five regions, its is possible to identify mitigation of sag levels through reconductoring only portions of the line. The ampacity for each of these line segments is calculated, and the limiting midpoint for each span at each time stamp is recorded for use in creating a histogram of the midpoints to look at the midpoint locations which cause the most frequent limiting calculations to the ampacity of the line. The data is analyzed for a full year from February of 2016 to February of 2017, the largest period for which all of the weather stations were functioning.

For the static rating, conservative assumptions are used for an ambient temperature of 40 ^{o}C, a maximum conductor temperature of 80 ^{o}C, a wind speed of 3.0 miles per hour, and solar heating rate of 1000 W/m^2 at a solar angle for the given latitude at noon on July 1, with a clear air assumption (usually valid due to the remoteness of the terrain), and a parallel angle of incidence for wind direction. For a substitute calculation on a Drake ASCR conductor, these parameters give a value for the static rating of about 600 A for the transmission line.

For each of the five line segments in the geographic location the minimum line ampacity is calculated at every 3-minute interval for which weather data is collected, and then a 15-minute moving average is applied. The ampacity is averaged rather than the raw weather data to avoid negating effects of parallel wind flow from nonlinear interactions of the cooling terms. The ampacity for the five line segments are shown in Fig. 8 (a) to (e). The data is plotted as the raw data collected at the weather stations with the azimuth of the nearest midpoint span compared to the data calculated using the corrected speed and incoming wind direction from the CFD results applied to each line midpoint span and taking the minimum of those values. From these raw ampacity plots, the difference between the CFD-corrected and raw weather station ampacity can be seen readily for most of the transmission line segments, except for section 1, where only minor difference is seen. Near the mouth of the canyon, the wind speed slow down effects are rather minor compared to the rest of the terrain. The 15 minute moving average is used as this is the approximate thermal relaxation time of a transmission line [6]. The minimum ampacity across all five of these line segments is shown in Fig. 8(f), most of the year the minimum ampacity is above the static rating, though the DLR calculation shows brief dips below the static rating during summer months, due to wind speeds occasionally dropping lower than assumptions made for the static rating.

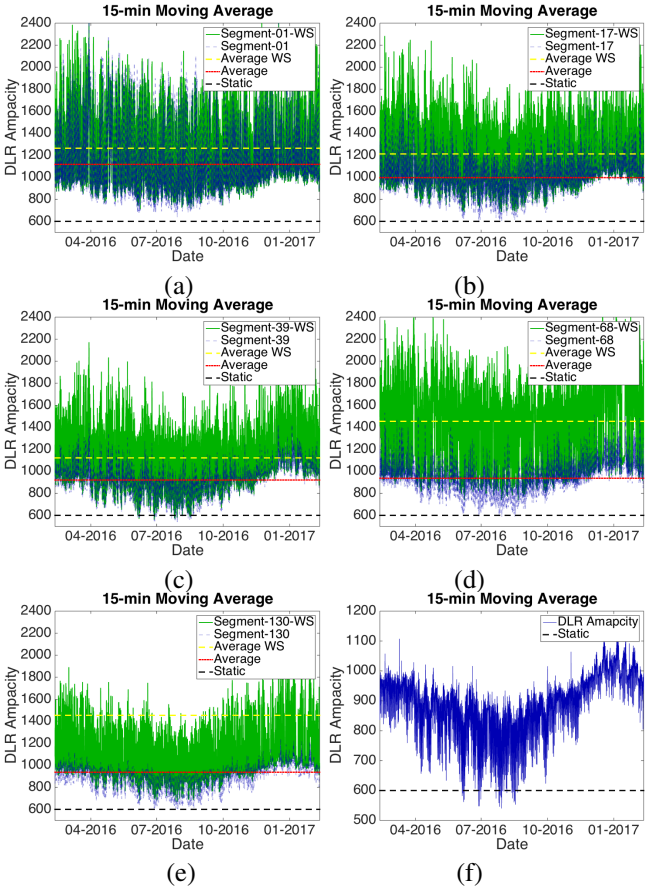

Fig. 8. Raw line ampacity values for the WS locations and the CFD corrected calculations compared to the static rating for segment 01 (a), 17 (b), 39 (c), 68 (d), and 130 (e). Dotted lines in these plots correspond to the time-averaged value of the ampacity. The minimum ampacity over at each timestamp is shown in (f).

The value of the dynamic rating over the ampacity is binned up so that the available headroom can be plotted as a function of the amount of time that the amount of headroom is available over the study period. This is plotted in Fig. 9 using both the data with the CFD corrected values applied to the midpoint spans, and for the value calculated using only the weather station data directly. The weather station data was used with only five azimuths corresponding to the weather station locations rather than the whole span. For using the weather station data, it was assumed the the midpoint azimuth was the transmission line span directly before the weather station structure location. Overall, dynamic line rating on this particular line provides an increase over the conservative static rating over 99% of the time during the study. However, the rating increase may be overestimated when only the weather station locations are considered, as no slow down of wind speed due to the hilly terrain is accounted for.

The average values for the year for the dynamic ampacity over the static rating are shown in Table III. These values are listed for both the data calculated with the GLASS code, and at the weather station locations without considering the CFD corrections. Most of the line segments show about a

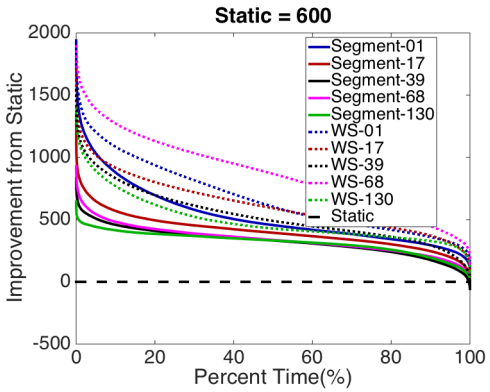

Fig. 9. The improvement in dynamic line rating over static rating for each of the line segments. Improvement over static at WS location only in dotted lines, solid lines include the CFD corrections to speeds.

150-200 A difference between using raw weather data and correcting it with CFD fields (about 30% of the static rating). The largest difference occurs with the 68 line segment at over a 500 A difference. This occurs as the location of this particular weather station is at the top of a ridge so it receives relatively high wind speeds, yet some of the midpoints of the transmission line associated with this weather station run through a valley that provides blocking of wind from the east-west incoming directions. Overall, the data show that there is much available headroom on the transmission line above the static rating. However, if the corrections from the CFD are not accounted for then the headroom available decreases from about double of the static ampacity down to about a 50% increase over static ampacity. It should be noted, even if a conservative derating is applied with the error shown in Table II, there would still be considerable headroom on this transmission line using DLR.

TABLE III
COMPARISON OF AMPACITY OVER STATIC RATING WITH AND WITHOUT CFD TABLES IN [A].

Line Section	Ampacity over static at WS	Ampacity over static with CFD
01	665	518
17	613	397
39	522	321
68	854	337
130	486	316

The variation in the calculated ampacity of individual line spans can vary as much as 3 times the static rating due to the large wind speed changes within the canyon. During summer months, occasionally low wind speeds cause natural convection to be more dominant in promoting heat loss from transmission lines than the forced convection from the wind. Much higher margins above static rating are seen in this transmission line during the winter months. This is mostly from higher convective cooling rates due to higher wind speeds in the winter, but also some contribution from the lower ambient temperatures. In addition, the higher winter ampacity also has some contributions from higher radiative heat loss and lower solar ampacity during the winter.

C. Limiting Midpoint Spans

Histograms are created of the limiting midpoints to show trends in which midpoints occur as limiting locations frequently. Refer to Fig. 3 for the locations of the midpoints, the numbers start in the south and increase when moving north. The wind roses for the five weather stations listed in the table are shown in Fig. 10. The red line in these plots marks the azimuth of the midpoint span closest to the weather station structure, and the turquoise region highlights the range of the azimuths for all midpoints associated with a given weather station. Several of these weather stations primarily show the wind flow over the year as mostly north-south direction with some bias towards the south west sector. This has a large impact on any calculations of ampacity made with the CFD based approach as the line runs primarily in the north-south direction. This means that the incidence angle correction factor of the wind speed cooling given by Eq. 10 will be rather small as most of the wind flows parallel to the line rather than perpendicular to it. It should be noted that WS39 and WS130 show much lower average wind speeds, and likely contribute towards the DLR sometimes dipping below the static rating.

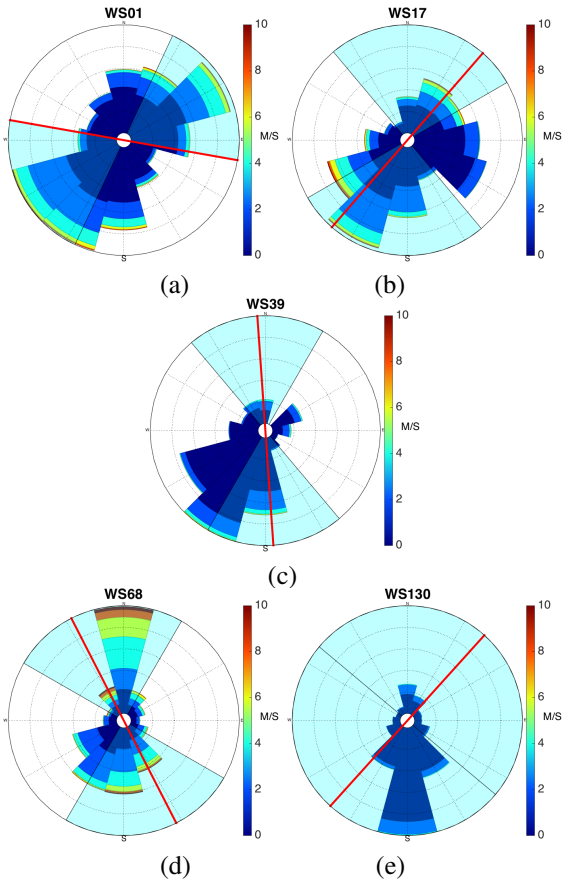

Fig. 10. Wind roses for five weather stations installed WS01 (a), WS17 (b), WS39 (c), WS68 (d) and WS130 (e).

While the limiting ampacity shown in Table III, seems to point to the northern 130 line segment as the main constriction

on the wind speeds, the data from GLASS can be analyzed further as it also indicates the limiting midpoints for each calculation. The percentage of time that each line segment is the limiting one is shown in Table IV. A majority of the limiting line segments lie in the northern three sections. The segment-130 occurs the most due to the very low wind speed conditions, and the segment-68 occurs primary from the transmission line direction proceeding mostly north-south aligned with the wind, along with the slowdown of wind speed from the east-west directions. This causes a 60% drop in the convective cooling term from the angle of incidence in Eq. 10, even though wind speeds are much higher at the top of the ridge. Similar effects occur with the segment 39 being aligned with the primary wind direction, as well as terrain providing wind speed reductions. This information could be utilized by a utility to re-conductor only portions of a transmission line which are limiting, rather than the entire region's transmission line. The breakdown is shown further in Fig. 11(a-e) with a histogram of the limiting midpoints for all five line segments as well as the histogram for the total limiting midpoint span among all of the segments in Fig. 11f. The overall histogram of the limiting midpoints along this line section show that there are a large number of limiting midpoints depending on the local weather conditions, and that while many are repeated, no singular midpoint along this short line section would be the limiting calculation for ampacity across the entire line for the studied time period.

TABLE IV
SUMMARY OF LIMITING LINE SEGMENTS FOR DYNAMIC LINE RATING.

Line Section	Percentage as limiting segment
01	3.08%
17	5.57%
39	29.28%
68	35.31%
130	27.22%

The maps in Fig. 12 highlight the specific locations of two of the midpoint locations on a contour plot of the elevation of the region. In Fig. 12a the midpoint 42 in the lower section of the canyon associated with the WS39 line segment is shown. The line in this region is at the bottom of the canyon running nearly parallel to the main wind direction recorded at the weather station. Similarly, in Fig. 12b the midpoint 100 in the upper section of the line is shown. As with the previous point this lies in a valley with significant slow down of east-west wind from the higher terrain, along with a parallel line direction. Other midpoints shown in the peaks of the histogram in Fig. 11f have similar characteristics.

The midpoints that show limiting effects have two major similarities – first, as expected many are in regions that lie near a ridge or in a valley which causes a decrease in wind speed from the terrain. The second is that the predominant wind direction relative to the azimuth is quite important. Several of the midpoint spans are nearly lined up with the predominant incoming wind sector. Due to the range of the K_{angle} variable from 0.38 up to 1.0, the angle of the wind direction with

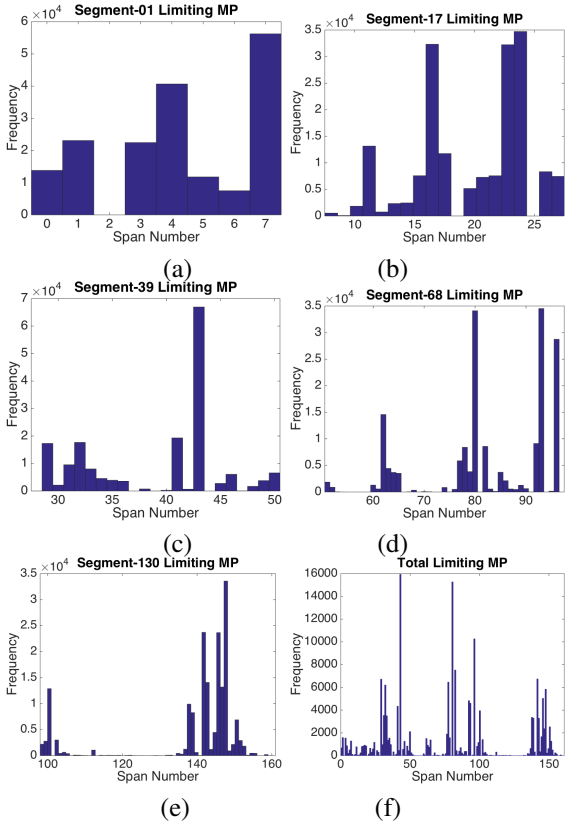

Fig. 11. Histograms of the limiting midpoint spans for segments (a) 01, (b) 17, (c) 39, (d) 68, (e) 130 and (f) Entire line.

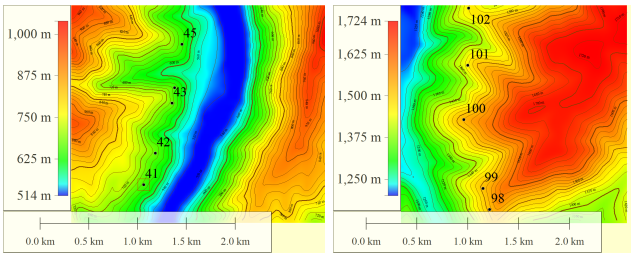

Fig. 12. Close up contour maps showing the elevation around limiting midpoints, centered near structures (a) 42 and (b) 100.

respect to the line segment azimuth — from perpendicular to parallel — can have a greater effect than halving the wind speed. The identification of the extent of the reduction of wind speed in specific areas is important in gathering information for the calculation of convective cooling in regions of complex terrain. However, the direction of the line segments relative to predominant wind direction is probably equally important in any potential planning and routing of new structures within the area.

V. CONCLUSION

Collected weather data over a year long span was used to calculated DLR ampacity, and showed a significant improvement over static rating assumptions for the studied transmission line. This weather data was coupled with CFD

results to provided corrections for slow wind speeds and changing wind directions. The data can also be used to find the most problematic midpoint span locations based on the low wind speed or parallel wind direction. While this may not be directly applicable to real-time dynamic line rating calculations, it may be of interest in future work using CFD for planning and routing tools, in order to avoid regions where transferred climatology data may show a significant drop in the wind speeds predicted elsewhere in the terrain of interest. A historical analysis of the use of dynamic line rating can identify future opportunity for implementation of the method to improve day-to-day operations. The analysis of the time-averaged data shows that midpoints, which have the azimuth line up with the incoming wind vector are usually the problematic spans, and when navigating lines through complex terrain, the wind rose direction frequency could be a consideration for the transmission path.

The results of the line segment analysis show that there can be a large difference between ampacity calculations based solely on weather data, and ampacity calculations considering local wind speeds from the CFD. Without applying the corrections to the wind field speeds and wind directions using the CFD results, applying the dynamic line rating can over predict the available headroom over the static rating. In addition, midpoint locations for potential installation of direct measurement devices can be identified by utilizing the CFD results to find the most frequent locations for limiting midpoint sections.

REFERENCES

[1] "Transmission facility rating methodology," Kansas City Power and Light Company, Tech. Rep., 2017.

[2] "Dynamic line rating systems for transmission lines: American recovery and reinvestment act of 2009," U.S. Department of Energy, Tech. Rep., 2014.

[3] "Smart grid system report," U.S. Department of Energy, Tech. Rep., 2010.

[4] "Guide for thermal rating calculations of overhead lines," CIGRE WG B2.43, Tech. Rep., 2014.

[5] "Overhead electrical conductors calculation methods for stranded bare conductors," IEC Standard TR 1597, Tech. Rep., 1985.

[6] "Standard for calculating current-temperature relationship of bare overhead line conductors," IEEE Standard 738, Tech. Rep., 2012.

[7] IEEE PES WG Subcommittee 15.11, "Real-time overhead transmission line monitoring for dynamic rating," *IEEE Trans. Power Deliv.*, vol. 31, no. 3, 2016.

[8] C. Y. Cong, P. Regulski, P. Wall, M. Osborne, and V. Terzija, "On the use of dynamic thermal-line ratings for improving operational tripping schemes," *IEEE Trans. Power Deliv.*, vol. 32, no. 4, pp. 1891–1900, 2016.

[9] E. F. Qiu and J. Wang, "Distributionally robust congestion management with dynamic line rating," *IEEE Trans. Power Syst.*, vol. 30, no. 4, pp. 2198–2199, 2015.

[10] L. Dawson and A. Knight, "Applicability of dynamic thermal line rating for long lines," *IEEE Trans. Power Deliv.*, vol. 33, no. 2, 2018.

[11] J. Gentle, "Concurrent wind cooling in power transmission lines," in *Western Energy Policy Research Conference*, August 2012.

[12] D. Greenwood and P. Taylor, "Investing the impact of real-time thermal ratings on power network reliability," *IEEE Trans. Power Syst.*, vol. 23, no. 5, pp. 2460–2468, 2014.

[13] J.-A. Jiang, Y.-T. Liang, C.-P. Chen, X.-Y. Zheng, C.-L. Chuang, and C.-H. Wang, "On dispatching line ampacities of power grids using weather-based conductor temperature forecasts," *IEEE Trans. Smart Grid*, vol. 9, no. 1, 2018.

[14] T. B. Phillips, I. Senocak, J. P. Gentle, M. K. S., and Anderson, "Investigation of a dynamic power line rating concept for improved wind energy integration over complex terrain," in *ASME 2014 4th Joint US-European Fluids Engineering Division Summer Meeting*, August 2014.

[15] B. P. Bhattarai, J. P. Gentle, P. Hill, T. McJunkin, K. S. Myers, A. Abboud, R. Renwick, and D. Hengst, "Transmission line ampacity improvements of altalink wind plant overhead tie-lines using weather-based dynamic line ratings," in *IEEE PES General Meeting*, July 2017.

[16] B. P. Bhattarai, J. P. Gentle, T. McJunkin, P. J. Hill, K. Myers, A. Abboud, and D. Hengst, "Improvement of transmission line ampacity utilization by weather-based dynamic line ratings," *IEEE Trans. Power Deliv.*, vol. 33, 2018, doi. 10.1109/TPWRD.2018.2798411.

[17] D. Greenwood, J. Gentle, K. Myers, P. Davison, I. West, J. Bush, G. Ingram, and M. Troffaes, "A comparison of real-time thermal rating systems in the u.s. and the u.k." *IEEE Trans. Power Deliv.*, vol. 29, no. 4, pp. 1849–1858, August 2014.

[18] B. J. L. Aznarte and N. Siebert, "Dynamic line rating using numerical weather predictions and machine learning: A case study," *IEEE Trans. Power Deliv.*, vol. 32, no. 1, pp. 335–343, 2017.

[19] Y. Yi, R. Harley, D. Divan, and T. Habetler, "Overhead conductor thermal dynamics identification by using echo state networks," in *Proc. Int. Joint Conf. Neural Netw.*, 2009, pp. 3426–3443.

[20] W. Jones and B. Launder, "The prediction of laminarization with a two-equation model of turbulence," *Int. J. Heat Mass Transf.*, vol. 15, no. 2, pp. 301–314, 1972.

[21] G. Bitsumalak, T. Stathopoulos, and C. Bedard, "Numerical evaluation of wind flow over complex terrain: Review," *J. of Aero. Eng.*, vol. 17, no. 4, pp. 135–145, 2004.

[22] T. Wallbank, "Windsim validation study: Cfd validation in complex terrain," Tech. Rep., 2008.

[23] A. Dhunny, M. Lollchund, and S. Rughooputh, "Numerical analysis of wind flow patterns over complex hilly terrains: comparison between two commonly used cfd

software," *Int. J. Glob. Energy Issues*, vol. 39, no. 3, pp. 181–203, 2016.

[24] S. Milashuk and W. Crane, "Wind speed prediction accuracy and expected errors of rans equations in low relief inland terrain for wind resource assessment purposes," *Environ. Model. Softw.*, vol. 26, pp. 429–433, 2011.

[25] A. Dhunny, M. Lollchund, and S. Rughooputh, "A high-resolution mapping of wind energy potentials for mauritus using computational fluid dynamics," *Wind Struct.*, vol. 20, no. 4, pp. 565–578, 2015.

[26] ——, "Wind energy evaluation for a highly complex terrain using computational fluid dynamics (cfd)," *Renew. Energy*, vol. 101, pp. 1–9, 2017.

[27] I. Toren and E. L. Petersen, *European Wind Atlas*. Risø National Laboratory, 1989.

[28] S. Koller and T. Humar, "Windpotentialanalyse fur windatlas jaresmittelwete der modellierten windgeschwindigkeit," Energieschweiz, Bern, Switzerland, Tech. Rep., 2016. [Online]. Available: http://www.bfe.admin.ch/geoinformation/05061/06675/index.html?lang=en&dossier_id=06606

[29] A. Michiorri, H. Nguen, S. Allessandrini, J. Bremnes, S. Dierer, E. Ferrero, B. Nygaard, P. Pinson, N. Thomaidis, and S. Uski, "Forecasting for dynamic line rating," *Renew. Sustain. Energy Rev.*, vol. 52, pp. 1713–1730, 2015.